nature photonics

AUGUST 2012 VOL 6 NO 8
www.nature.com/naturephotonics

X-RAY FREE-ELECTRON LASERS
Sub-ångström lasing

IMAGING
Looking around corners

PHOTOVOLTAICS
Dye-sensitized upconversion

Graphene–silicon optoelectronics

ARTICLES
PUBLISHED ONLINE: 15 JULY 2012 | DOI: 10.1038/NPHOTON.2012.147
nature photonics

Regenerative oscillation and four-wave mixing in graphene optoelectronics

T. Gu[1]*, N. Petrone[2], J. F. McMillan[1], A. van der Zande[2], M. Yu[3], G. Q. Lo[3], D. L. Kwong[3], J. Hone[2] and C. W. Wong[2]*

The unique linear and massless band structure of graphene in a purely two-dimensional Dirac fermionic structure has led to intense research in fields ranging from condensed matter physics to nanoscale device applications covering the electrical, thermal, mechanical and optical domains. Here, we report three consecutive first observations in graphene–silicon hybrid optoelectronic devices—ultralow-power resonant optical bistability, self-induced regenerative oscillations and coherent four-wave mixing—all at few-femtojoule cavity recirculating energies. These observations, in comparison with control measurements on solely monolithic silicon cavities, are enabled only by the dramatically large and ultrafast $\chi^{(3)}$ nonlinearities in graphene and the large Q/V ratios in wavelength-localized photonic crystal cavities. These third-order nonlinear results demonstrate the feasibility and versatility of hybrid two-dimensional graphene–silicon nanophotonic devices for next-generation chip-scale high-speed optical communications, radiofrequency optoelectronics and all-optical signal processing.

Subwavelength nanostructures in monolithic material platforms have been the subject of rapid advances in the development of chip-scale optoelectronic modulators[1–4], photoreceivers[5,6] and high-bit-rate signal-processing architectures[7,8]. Coupled with ultrafast nonlinearities as a new parameter space for optical physics[9], breakthroughs such as resonant four-wave mixing[10] and parametric femtosecond pulse characterization[11,12] have been described. Graphene—with its broadband dispersionless nature and large carrier mobility—has recently been investigated for its physical[13–17] and device properties[18–24]. The unique gate-variable optical transitions[25,26] allows graphene an ideal material platform for broadband electro-absorption modulators[27] and photoreceivers[28,29], including planar microcavity-enhanced photodetectors[30,31], as well as saturable absorption for mode-locking[32]. Because its linear band structure allows interband optical transitions at all photon energies, graphene has been suggested as a material that might have large $\chi^{(3)}$ nonlinearities[33].

In this Article, we demonstrate the exceptionally high third-order nonlinear response of graphene with a wavelength-scale localized photonic crystal cavity, enabling ultralow-power optical bistable switching, self-induced regenerative oscillations and coherent four-wave mixing at femtojoule cavity energies on a semiconductor chip platform. For this purpose we examined a hybrid graphene–silicon cavity (Fig. 1), fabricated by the rigorous transfer of a monolayer large-area graphene sheet onto air-bridged silicon photonic crystal nanomembranes with minimal linear absorption and optimized optical input/output coupling. This optoelectronics demonstration complements recent investigations of large-area[34,35] graphene field-effect transistors and analogue circuit designs[36] for potential large-scale silicon integration.

Figure 1 shows our graphene-clad photonic crystal nanomembranes. The optical nanocavity is a point-defect photonic crystal $L3$ cavity (with three missing holes)[35,36], with the nearest holes at the cavity edges tuned by $0.15a$ (where a is the photonic crystal lattice constant). The $L3$ cavity was side-coupled to a photonic crystal line defect waveguide for optical transmission measurements. Heavily p-doped graphene grown by chemical vapour deposition (CVD) was wet-transferred onto the silicon nanomembrane[39,40] (see Methods and Supplementary Section S1) as a large sheet, without requiring precise alignment. As shown in Fig. 1b, the single-layer graphene was identified by Raman spectroscopy from the full-width at half-maximum (FWHM) of the G and 2D band peaks (34.9 cm^{-1} and 49.6 cm^{-1} respectively) and the G-to-2D peak intensity ratio (~1–1.5). The G-band lineshape is a single and symmetrical Lorentzian, indicating graphene with good uniformity[41]. Heavily doped graphene was specifically prepared to achieve optical transparency in the infrared with negligible linear losses, as the Fermi level is below the one-photon interband optical transition threshold[27] (Fig. 1c, inset) and intraband graphene absorption is near-absent in the infrared[42].

Laser light with transverse electric (TE) polarization was launched into the optical cavity and evanescently coupled to the monolayer graphene. The cavity transmission spectra, obtained with tunable continuous-wave laser sources at 0.6 mW, show a consistent and large resonance redshift of 1.2 nm mW^{-1} (Fig. 1d), approximately four times larger than that of our near-identical control cavity without graphene (more measurements are provided in Supplementary Section S3). The low-power 'cold-cavity' transmissions measured at an input power of 2.5 μW show intrinsic Q-values of 23,000 and loaded Q-values of 7,500, with background Fabry–Pérot oscillations arising from the input/output facet coupling reflections (reflectivity of ~0.12). The high-power cavity transmission is not only redshifted to lie outside the cold-cavity lineshape full-width base, but also exhibits a Fano-like asymmetric lineshape, with good matching to our coupled-mode model predictions (Supplementary Section S3). We also note that with the monolayer graphene transferred only onto the short photonic crystal regions, the total fibre–chip–fibre transmission is reduced by less than 1 dB, which is slightly better than the 5 dB additional loss observed in recent modified graphene-fibre linear polarizers[43] (with different

[1]Department of Electrical Engineering, Columbia University, New York, New York 10027, USA, [2]Department of Mechanical Engineering, Columbia University, New York, New York 10027, USA, [3]The Institute of Microelectronics, 11 Science Park Road, Singapore Science Park II, Singapore 117685, Singapore.
*e-mail: tg2342@columbia.edu; cww2104@columbia.edu

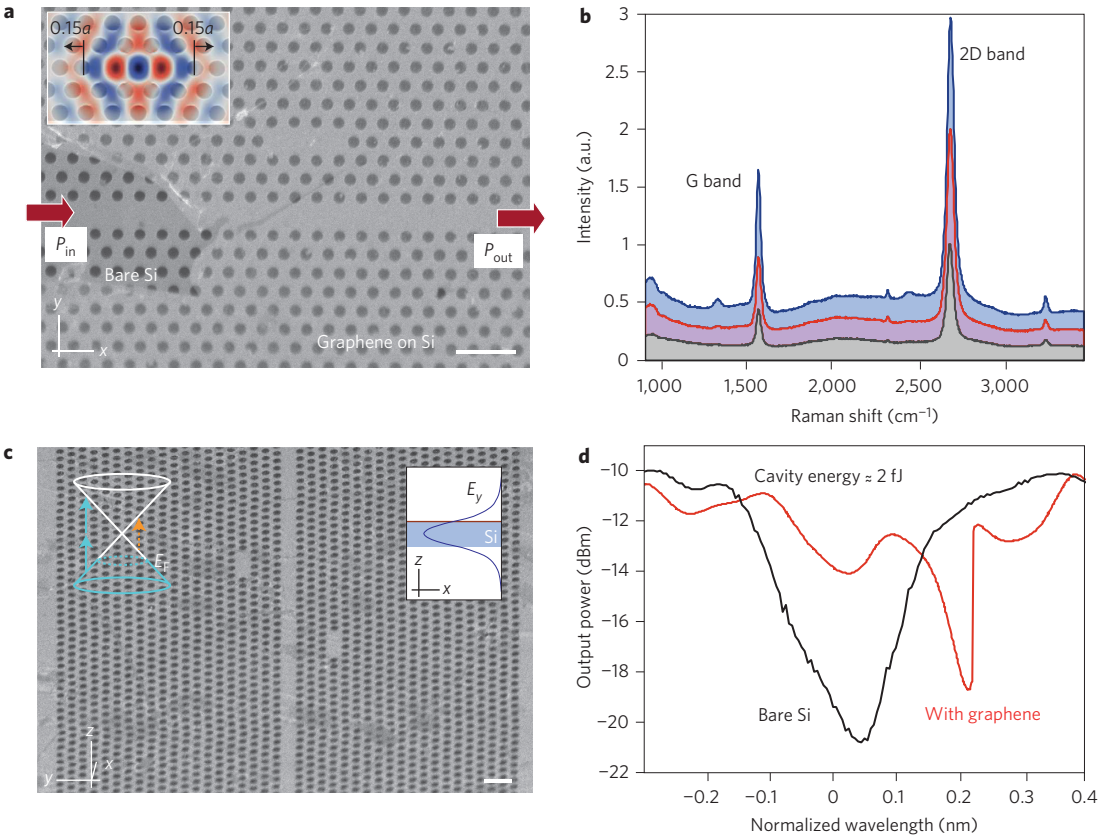

Figure 1 | Graphene-clad silicon photonic crystal nanostructures. a, Scanning electron micrograph (SEM) of the tuned photonic crystal cavity, with lattice constant $a = 420$ nm. Example SEM with separated graphene monolayer on silicon for illustration. Scale bar, 500 nm. Inset: example E_z-field from finite-difference time-domain computations. **b**, Measured Raman scattering spectra of monolayer CVD-grown graphene on the photonic crystal cavity membrane. The Lorentzian lineshape FWHM of the G-band (34.9 cm^{-1}) and 2D-band (49.6 cm^{-1}) peaks and the G-to-2D peak ratio indicate that the graphene is monolayer, and the single symmetric G peak indicates good uniformity of the graphene. Homogeneity across the sample was examined by excitation at different locations across the cavity membrane (blue, red and grey). **c**, SEM of the suspended graphene–silicon membrane. Dark patches represent bilayer graphene. Left inset: Dirac cone illustrating the highly doped Fermi level (dashed blue circle), allowing the two-photon transition (blue arrows) but forbidding the one-photon transition (orange dashed arrow). Right inset: computed E_y-field along the z-direction, with graphene at the evanescent top interface. Scale bar, 500 nm. **d**, Example measured graphene-clad cavity transmission with asymmetric Fano-like lineshapes (red line) and significantly larger redshift compared to a control bare silicon cavity sample with symmetric Lorentzian lineshapes (black line). Both spectra were measured with an input power of 0.6 mW, and are centred to the intrinsic cavity resonances ($\lambda_{cavity\_0} = 1{,}562.36$ nm for the graphene sample and $\lambda_{cavity\_0} = 1{,}557.72$ nm for the silicon sample), measured at low power (input power <100 μW). The intrinsic cavity quality factors of the graphene and control samples are similar.

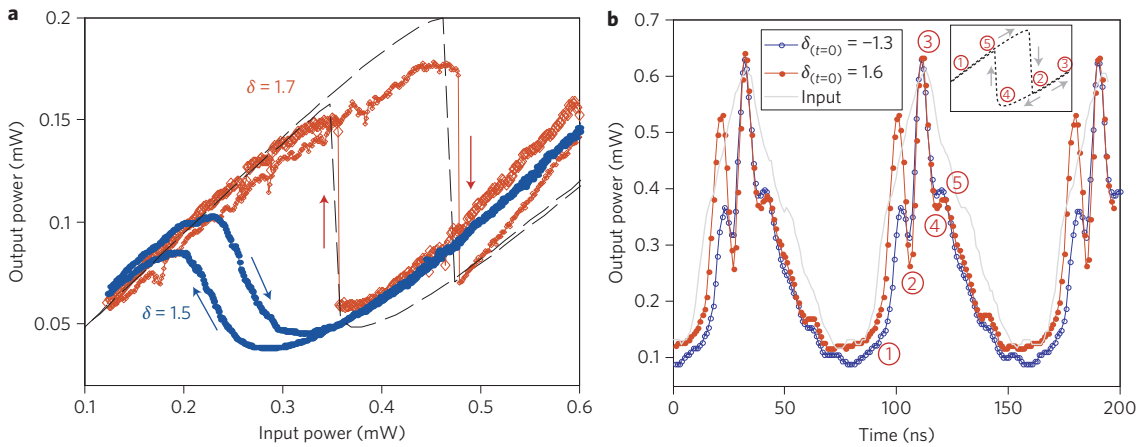

Figure 2 | Bistable switching in graphene-clad nanocavities. a, Steady-state input/output optical bistability for the quasi-TE cavity mode with laser-cavity detuning of $\delta = 1.5$ ($\lambda_{laser} = 1{,}562.66$ nm) and 1.7 ($\lambda_{laser} = 1{,}562.70$ nm). The dashed black line represents the coupled-mode theory simulation with effective nonlinear parameters for the graphene–silicon cavity sample. **b**, Switching dynamics with triangular-waveform drive input (dashed grey line). Bistable resonances are observed for both positive and negative detuning. Blue open circles, $\delta_{(t=0)} = -1.3$ ($\lambda_{laser} = 1{,}562.10$ nm); red filled circles, $\delta_{(t=0)} = 1.6$ ($\lambda_{laser} = 1{,}562.68$ nm). Inset: schematic of high- and low-state transmissions.

cavity or propagation lengths and evanescent core coupling). We emphasize that, with the same increased cavity power on a monolithic silicon cavity without graphene, both the control experiment and numerical models show a negligible thermal redshift of 0.1 nm mW^{-1} for the power levels and specific loaded cavity Q^2/V values ($4.3 \times 10^7(\lambda/n)^{-3}$) investigated here.

The large frequency shifts from the graphene-clad hybrid photonic cavity were next investigated for low-threshold optical bistability. Figure 2a shows the observed bistability at threshold powers of 100 μW for a loaded cavity Q of 7,500 ($Q_{intrinsic} = 23{,}000$), with cavity-input laser detuning of $\delta = 1.5$ (where $\delta = (\lambda_{laser} - \lambda_{cavity})/\Delta\lambda_{cavity}$ and $\Delta\lambda_{cavity}$ is the cold-cavity FWHM linewidth). The steady-state bistable hysteresis at $\delta = 1.7$ is also illustrated in Fig. 2a. The dashed lines show the numerical predictions of coupled-mode theory for the hybrid cavity, including first-order estimates of the graphene-modified thermal, linear and nonlinear losses, and free carrier parameters (detailed in Supplementary Sections S2,S3). We also note that the heavily doped graphene has a two-photon absorption at least several times larger than silicon, described by its isotropic bands for interband optical transitions[43], leading to increased free carrier densities/absorption and overall enhanced thermal redshift.

To verify the bistable switching dynamics, we input time-varying intensities to the graphene-clad cavity, allowing a combined cavity power–detuning sweep. Figure 2b presents an example of a time-domain output transmission for two different initial detunings ($\delta_{(t=0)} = -1.3$ and $\delta_{(t=0)} = 1.6$) and for an illustrative triangular-waveform drive, on an amplified photoreceiver with nanosecond resolution. With a drive period of 77 ns, the observed thermal relaxation time is ~40 ns. Cavity resonance dips (with modulation depths of ~3 dB in this example) are observed for both positive detuning (up to 0.34 nm, [$\delta = 1.4$]) and negative detuning (from −0.15 nm [$\delta = -0.75$] to −0.10 nm [$\delta = -0.5$]). The respective two-state high- and low-state transmissions are illustrated in the inset of Fig. 2b for each switching cycle. With negative detuning and triangular pulses, the carrier-induced (Drude) blueshifted dispersion overshoots the cavity resonance from the drive frequency, then thermally pins the cavity resonance to the laser drive frequency (for details see Supplementary Section S4). Because the free-carrier lifetime of the hybrid media is ~200 ps and therefore significantly shorter than the duration of the drive pulse, these series of measurements are thermally dominated; the clear (attenuated) resonance dips on the intensity up-sweeps (down-sweeps) are a

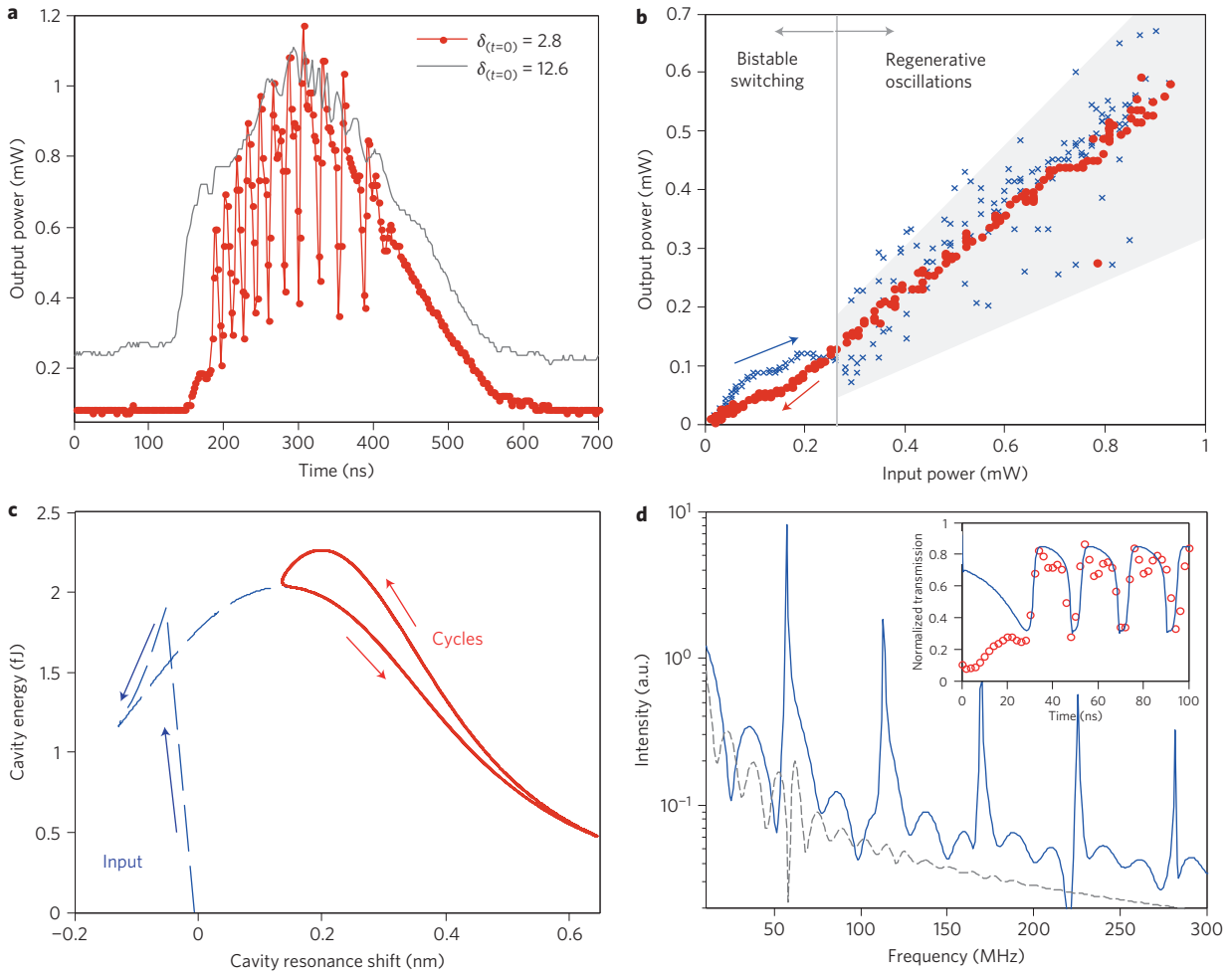

Figure 3 | Regenerative oscillations in graphene-clad nanocavities. a, Observations of temporal regenerative oscillations in the cavity for optimized detuning ($\lambda_{laser} = 1{,}562.47$ nm). The input power has a quasi-triangular waveform with peak power of 1.2 mW. The grey line is the reference output power, with the laser further detuned at 1.2 nm from cavity resonance ($\lambda_{laser} = 1{,}563.56$ nm). **b**, Mapping of output power versus input power with slow up (blue crosses) and down (red circles) power sweeps. In the up-sweep process, the cavity starts to oscillate when the input power is beyond 0.29 mW. **c**, Nonlinear coupled-mode theory model of cavity transmission versus resonance shift, in the regime of regenerative oscillations. With a detuning of 0.15 nm ($\delta_{(t=0)} = 0.78$) the free carrier density swings from 4.4 to 9.1×10^{17} cm^{-3} and the increased temperature ΔT circulates between 6.6 and 9.1 K. **d**, Radiofrequency spectrum of output power below (0.4 mW, grey dashed line) and above (0.6 mW, blue solid line) oscillation threshold at the same detuning $\delta_{(t=0)} = 0.78$ ($\lambda_{laser} - \lambda_{cavity} =$ 0.15 nm), as in **c**. Inset: normalized transmission from the model (blue line) and experimental data (red circles) at the same constant power level.

result of the measurement sampling time being shorter than the timescale of thermal relaxation and the cooler (hotter) initial cavity temperature.

When the input laser intensity is well above the bistability threshold, the graphene-cavity system deviates from two-state bistable switching and becomes oscillatory (Fig. 3a). Regenerative oscillation has only been suggested in a few other studies. For example, it has been theoretically predicted in GaAs nanocavities with large Kerr nonlinearities[44] and has been observed in high-Q (3×10^5) silicon microdisks[45]. These regenerative oscillations are formed between competing phonon and free-carrier populations, with slow thermal redshifts (timescales of ~10 ns) and fast free-carrier plasma dispersion blueshifts (timescales of ~200 ps) in the case of our graphene–silicon cavities. Self-induced oscillations across the drive laser frequency are observed at threshold cavity powers of 0.4 mW and with periods of ~9.4 ns in these series of measurements (giving modulation rates of ~106 MHz), at experimentally optimized detunings from $\delta_{(t=0)} = 0.68$ to 1.12. We emphasize that, for a monolithic silicon $L3$ cavity, such regenerative pulsation has not been observed and is not predicted to be observable at a relatively modest Q of 7,500 (Supplementary Section S4).

Figure 3b presents input–output intensity cycles constructed from the temporal response measurements of a triangular-wave modulated 1.2 mW laser with a 2 μs cycle. Clear bistability behaviour is seen below the carrier oscillation threshold. The system transits to the regime of self-sustained oscillations as the power coupled into the cavity increases above threshold, by tuning the laser wavelength into cavity resonance. Figure 3c shows an illustrative example of numerical modelling in which the fast free-carrier response fires the excitation pulse (blue dashed line, start cycle), and heat diffusion (red solid line), with its slower time constant, determines the recovery to the quiescent state in the graphene-clad suspended silicon membrane. The beating rate between the thermal and free-carrier dynamics is ~50 MHz, as shown in the inset of Fig. 3d, which matches the experimental data and coupled-mode theory simulation. The beating gives rise to tunable peaks in the radiofrequency spectra (Fig. 3d; blue solid line), which are absent when the input power is below the oscillation threshold (grey dashed line).

To examine only the Kerr nonlinearity, we next performed degenerate four-wave mixing measurements on the hybrid graphene–silicon photonic crystal cavities (Fig. 4) with a continuous-wave laser input. A lower bound Q of 7,500 was specifically chosen to

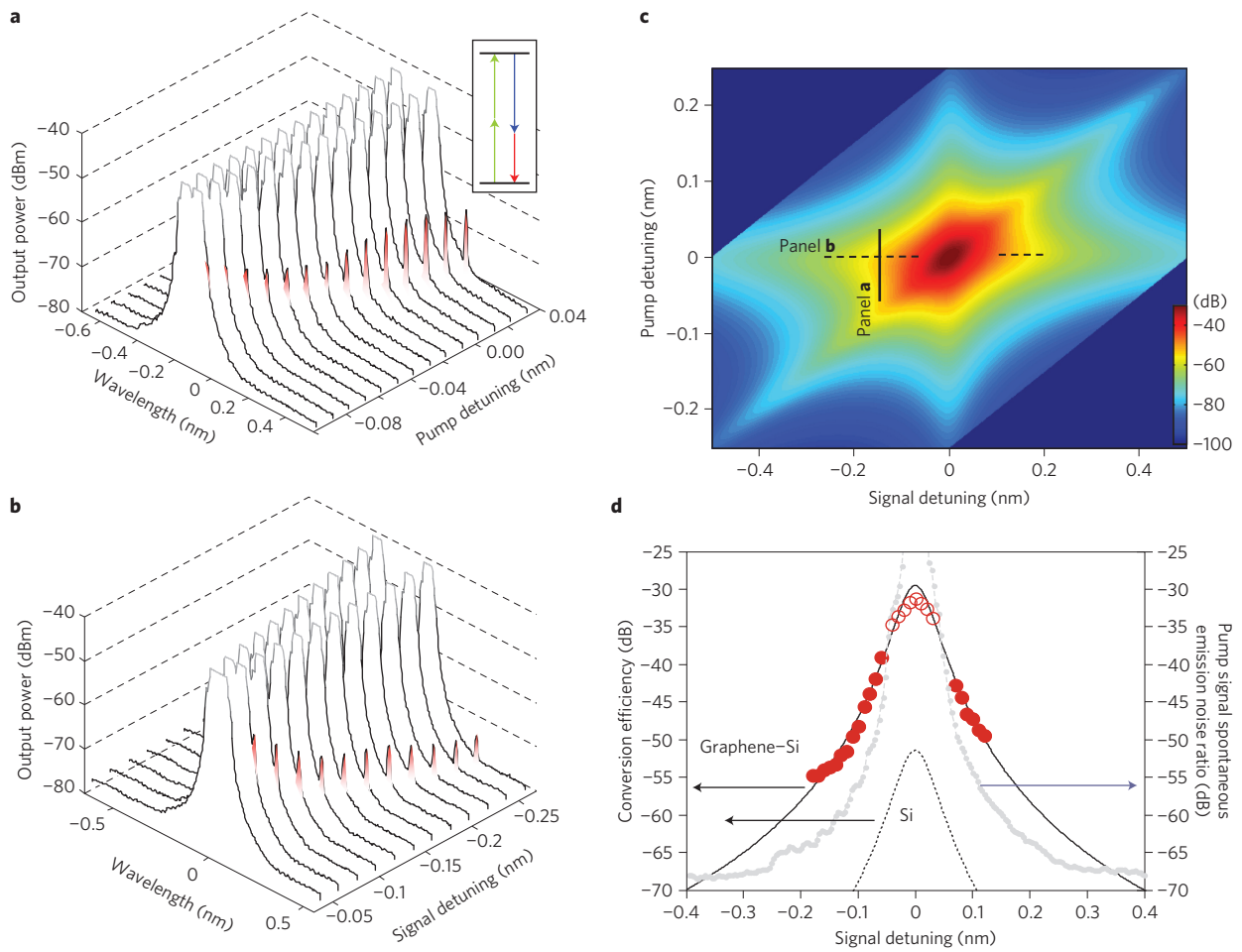

Figure 4 | Parametric four-wave mixing in graphene-clad silicon nanocavities. a, Measured transmission spectrum with signal laser fixed at −0.16 nm according to cavity resonance wavelength, while scanning the pump laser detuning from −0.1 to 0.03 nm. Inset: band diagram of the degenerate four-wave mixing process with pump (green), signal (blue) and idler (red) lasers. **b**, Measured transmission spectrum with pump laser fixed on cavity resonance, and signal laser detuning scanned from −0.04 to −0.27 nm. **c**, Modelled conversion efficiency versus pump and signal detuning from the cavity resonance. The solid and dashed lines mark the regions plotted in **a** and **b**, respectively. **d**, Observed and simulated conversion efficiencies of the cavity. Red filled dots are measured with signal detuning as in **b**, and open circles are obtained with pump detuning as in **a**, plus 29.5 dB (offset due to the 0.16 nm signal detuning). Solid and dashed black lines are modelled conversion efficiencies for the graphene–silicon and monolithic silicon cavities, respectively. Grey dashed line (superimposed): illustrative pump/signal laser spontaneous emission noise ratio.

allow a cavity linewidth of ~200 pm, within which the highly dispersive four-wave mixing could be examined. The input pump and signal laser detunings were placed within this linewidth, with matched TE-like input polarization, and the powers were set at 600 μW. Two example series of idler measurements are presented in Fig. 4a,b, with differential pump and signal detunings, respectively. In both series, the parametric idler is clearly observed as a sideband to the cavity resonance, with the pump detuning ranging from −100 pm to 30 pm and the signal detuning ranging from −275 pm to −40 pm, and from 70 pm to 120 pm (shown in Fig. 4d). For each fixed signal- and pump-cavity detuning, the generated idler shows a slight intensity roll-off from linear signal (or pump) power dependence when the transmitted signal (or pump) power is greater than ~400 μW due to increasing free-carrier absorption effects (Supplementary Fig. S5). As illustrated in Fig. 4a,b, the converted idler wave shows a four-wave mixing 3 dB bandwidth roughly matching the cavity linewidth when the pump laser is centred on the cavity resonance.

A theoretical four-wave mixing model with cavity field enhancement (Fig. 4c,d) matches these first graphene-cavity observations, and is described in further detail in Supplementary Section S5. Based on the match of the numerical model to the experimental observations, the observed Kerr coefficient n_2 of the graphene–silicon cavity ensemble is 4.8×10^{-17} m^2 W^{-1}, an order of magnitude larger than in monolithic silicon and GaInP-related materials[12], and two orders of magnitude larger than in silicon nitride[25]. Independently, we also modelled the field-averaged effective $\chi^{(3)}$ and n_2 of the hybrid graphene–silicon cavity, described as

$$\overline{n_2} = \left(\frac{\lambda_0}{2\pi}\right)^d \frac{\int n^2(r) n_2(r)(|E(r)\cdot E(r)|^2 + 2|E(r)\cdot E^*(r)|^2)\mathrm{d}^d r}{(\int n^2(r)|E(r)|^2 \mathrm{d}^d r)^2}$$

where $E(r)$ represents the complex fields in the cavity, $n(r)$ is the local refractive index, λ_0 is the wavelength in vacuum, and d is the number of dimensions (three). As detailed in Supplementary Section S5, the computed n_2 is 7.7×10^{-17} m^2 W^{-1}, which closely matches the observed n_2 derived from four-wave mixing. For both measurement and theory (Fig. 4d), the derived conversion efficiencies are observed up to −30 dB in the unoptimized graphene cavity, even at cavity Q-values of 7,500 and low pump powers of 600 μW. Highly doped graphene with the Fermi level in the optical transparency region is a prerequisite to these observations. We note that for a silicon cavity without graphene the conversion efficiencies are dramatically lower (by more than 20 dB), shown by the dashed black line in Fig. 4d, and even below the pump/signal laser spontaneous emission noise ratio (dotted grey line), preventing the observation of four-wave mixing in a single monolithic silicon photonic crystal cavity until now.

We have demonstrated, for the first time, a hybrid graphene–silicon optical cavity for chip-scale optoelectronics, with third-order nonlinear observations ranging from resonant optical bistability for optical signal processing at femtojoule-level switching per bit, to temporal regenerative oscillations at record femtojoule cavity circulating powers for optically driven and controlled reference oscillators, and to graphene-cavity enhanced four-wave mixing at femtojoule energies on the chip. The transferred graphene on a wavelength-scale localized optical cavity enhances not only the thermal nonlinearities, but also the ultrafast effective Kerr nonlinearity, suggesting a new parameter space for chip-scale optical physics and ultrafast optics in optical information processing.

Methods

Device fabrication. Photonic crystal nanostructures were defined by 248 nm deep-ultraviolet lithography in a silicon CMOS foundry on undoped silicon-on-insulator (100) substrates. Optimized lithography and reactive ion etching were used to produce device lattice constants of 420 nm, and a hole radius of 124±2 nm. The photonic crystal cavities and waveguides were designed and fabricated on a silicon device with a thickness of 250 nm, followed by a buffered hydrofluoric wet etch of the 1 μm buried oxide to achieve the suspended photonic crystal nanomembranes.

Centimetre-scale graphene was grown on 25-μm-thick copper foils by CVD of carbon. To achieve this, the top oxide layer of the copper was removed in a hydrogen atmosphere (50 mtorr, 1,000 °C, 2 s.c.c.m. H_2 for 15 min), and monolayer carbon was then formed on the copper surface (250 mtorr, 1,000 °C, 35 s.c.c.m CH_4, 2 s.c.c.m. H_2 for 30 min). The growth was self-limiting, terminating as soon as the copper surface catalyst was covered by carbon atoms. The single-layer graphene was then cooled rapidly before being removed from the chamber. Poly(methyl methacrylate) (PMMA) was then spincast onto the graphene and the copper foil etch-removed by floating the sample in $FeNO_3$ solution. After removal of the metal, the graphene was transferred to a water bath before subsequent transfer onto the photonic crystal membranes. Acetone was used to dissolve the PMMA layer, and the sample was rinsed with isopropyl alcohol and dry-baked before measurements.

Optical measurements. Continuous-wave finely tuned semiconductor lasers with wavelengths from 1,520 to 1,620 nm (200 kHz bandwidth and −20 to 7 dBm powers) were used for the measurements, as well as lensed tapered fibres (Ozoptics) with polarization controller and integrated on-chip spot size converters. Without graphene cladding (control sample), the total fibre–chip–fibre transmission was approximately −10 dB. The fibre-to-channel waveguide coupling was optimized to be 3 dB per input/output facet, with 1–2 dB loss from channel to photonic crystal waveguide coupling. The linear propagation loss for our air-clad photonic crystal waveguide was determined to be 0.6 dB mm^{-1}, and for a photonic crystal waveguide length of 0.12 mm the propagation loss in the waveguide was negligible. The output was monitored by an amplified InGaAs photodetector (Thorlabs PDA10CF, DC—150 MHz bandwidth) and oscilloscope (WaveJet 314A, 100 MHz bandwidth, 3.5 ns rise time) for the time-domain oscillations. The four-wave mixing pump laser linewidth was 10 pm (~1.2 GHz). Confocal microscopy was used for the graphene Raman spectroscopic measurements, with a ×100 (NA 0.95) objective, pumped with a 514 nm laser.

Numerical simulations. A three-dimensional finite-difference time-domain (FDTD) method with sub-pixel averaging was used to calculate the real and imaginary parts of the E-field distribution for the cavity resonant mode. The spatial resolution was set at 1/30 of the lattice constant (14 nm). Time-domain coupled-mode theory, including free-carrier dispersion with dynamics and thermal time constants, was carried out with a temporal resolution of 1 ps.

Received 6 February 2012; accepted 23 May 2012; published online 15 July 2012

References

1. Xu, Q., Schmidt, B., Pradhan, S. & Lipson, M. Micrometre-scale silicon electro-optic modulator. *Nature* **435,** 325–327 (2005).
2. Liu, A. *et al.* A high-speed silicon optical modulator based on a metal–oxide–semiconductor capacitor. *Nature* **427,** 615–618 (2005).
3. Liu, J. *et al.* Waveguide-integrated, ultralow-energy GeSi electro-absorption modulators. *Nature Photon.* **2,** 433–437 (2008).
4. Kuo, Y.-H. *et al.* Strong quantum-confined Stark effect in germanium quantum-well structures on silicon. *Nature* **437,** 1334–1336 (2005).
5. Assefa, S., Xia, F. & Vlasov, Y. A. Reinventing germanium avalanche photodetector for nanophotonic on-chip optical interconnects. *Nature* **464,** 80–84 (2010).
6. Kang, Y. *et al.* Monolithic germanium/silicon avalanche photodiodes with 340 GHz gain–bandwidth product. *Nature Photon.* **3,** 59–63 (2009).
7. Biberman, A. *et al.* First demonstration of long-haul transmission using silicon microring modulators. *Opt. Express* **18,** 15544–15552 (2010).
8. Pelusi, M. *et al.* Photonic-chip-based radio-frequency spectrum analyser with terahertz bandwidth. *Nature Photon.* **3,** 139–143 (2009).
9. Colman, P. *et al.* Temporal solitons and pulse compression in photonic crystal waveguides. *Nature Photon.* **4,** 862–868 (2010).
10. Morichetti, F. *et al.* Travelling-wave resonant four-wave mixing breaks the limits of cavity-enhanced all-optical wavelength conversion. *Nature Commun.* **2,** 296 (2011).
11. Foster, M. *et al.* Silicon-chip-based ultrafast optical oscilloscope. *Nature* **456,** 81–84 (2008).
12. Pasquazi, A. M. *et al.* Sub-picosecond phase-sensitive optical pulse characterization on a chip. *Nature Photon.* **5,** 618–623 (2011).
13. Zhang, Y., Tan, Y.-W., Stormer, H. L. & Kim, P. Experimental observation of the quantum Hall effect and Berry's phase in graphene. *Nature* **438,** 201–204 (2005).
14. Geim, A. K. & Novoselov, K. S. The rise of graphene. *Nature Mater.* **6,** 183–191 (2007).
15. Du, X. *et al.* Fractional quantum Hall effect and insulating phase of Dirac electrons in graphene. *Nature* **462,** 192–195 (2009).
16. Dean, C. R. *et al.* Multicomponent fractional quantum Hall effect in graphene. *Nature Phys.* **7,** 693–696 (2011).

17. Berger, C. *et al.* Electronic confinement and coherence in patterned epitaxial graphene. *Science* **312,** 1191–1196 (2006).
18. Meric, I. *et al.* Current saturation in zero-bandgap, top-gated graphene field-effect transistors. *Nature Nanotech.* **3,** 654–659 (2008).
19. Lin, Y.-M. *et al.* 100-GHz transistors from wafer-scale epitaxial graphene. *Science* **327,** 662 (2010).
20. Seol, J. H. *et al.* Two-dimensional phonon transport in supported graphene. *Science* **328,** 213–216 (2010).
21. Gabor, N. M. *et al.* Hot carrier-assisted intrinsic photoresponse in graphene. *Science* **334,** 648–652 (2011).
22. Lee, C., Wei, X., Kysar, J. W. & Hone, J. Measurement of the elastic properties and intrinsic strength of monolayer graphene. *Science* **321,** 385–388 (2008).
23. Bonaccorso, F., Sun, Z., Hasan, T. & Ferrari, A. C. Graphene photonics and optoelectronics. *Nature Photon.* **4,** 611–622 (2010).
24. Chen, C.-F. *et al.* Controlling inelastic light scattering quantum pathways in graphene. *Nature* **471,** 617–620 (2011).
25. Wang, F. *et al.* Gate-variable optical transitions in graphene. *Science* **320,** 206–209 (2008).
26. Li, Z. Q. *et al.* Dirac charge dynamics in graphene by infrared spectroscopy. *Nature Phys.* **4,** 532–535 (2008).
27. Liu, M. *et al.* A graphene-based broadband optical modulator. *Nature* **474,** 64–67 (2011).
28. Mueller, T., Xia, F. & Avouris, P. Graphene photodetectors for high-speed optical communications. *Nature Photon.* **4,** 297–301 (2010).
29. Xia, F. *et al.* Ultrafast graphene photodetector. *Nature Nanotech.* **4,** 839–843 (2009).
30. Engel, M. *et al.* Light–matter interaction in a microcavity-controlled graphene transistor. *Nature Commun.* **3,** 906 (2012).
31. Furchi, M. *et al.* Microcavity-integrated graphene photodetector. *Nano Lett.* **12,** 2773–2777 (2012).
32. Sun, Z. *et al.* Graphene mode-locked ultrafast laser. *ACS Nano* **4,** 803–810 (2010).
33. Hendry, E. *et al.* Coherent nonlinear optical response of graphene. *Phys. Rev. Lett.* **105,** 097401 (2010).
34. Li, X. *et al.* Large-area synthesis of high-quality and uniform graphene films on copper foils. *Science* **324,** 1312–1314 (2009).
35. Bae, S. *et al.* Roll-to-roll production of 30-inch graphene films for transparent electrodes. *Nature Nanotech.* **5,** 574–578 (2010).
36. Lin, Y.-M. *et al.* Wafer-scale graphene integrated circuit. *Science* **332,** 1294–1297 (2011).
37. Akahane, Y., Asano, T., Song, B. & Noda S. High-*Q* photonic nanocavity in a two-dimensional photonic crystal. *Nature* **425,** 944–947 (2003).
38. Yang, X., Yu, M., Kwong, D.-L. & Wong, C. W. All-optical analogue to electromagnetically induced transparency in multiple coupled photonic crystal cavities. *Phys. Rev. Lett.* **102,** 173902 (2009).
39. Dean, C. R. *et al.* Boron nitride substrate for high-quality graphene electronics. *Nature Nanotech.* **5,** 722–726 (2010).
40. Petrone, N. *et al.* High-mobility scalable graphene by large-grain chemical vapor deposition growth. *Nano Lett.* **12,** 2751–2756 (2012).
41. Zhao, W., Tan, P. H., Liu, J. & Ferrari, A. C., Intercalation of few-layer graphite flakes with $FeCl_3$: Raman determination of Fermi level, layer by layer decoupling and stability. *J. Am. Chem. Soc.* **133,** 5941–5946 (2011).
42. Jablan, M., Buljan, H. & Soljačić, M. Plasmonics in graphene at infrared frequencies. *Phys. Rev. B* **80,** 245435 (2009).
43. Bao, Q. *et al.* Broadband graphene polarizer. *Nature Photon.* **5,** 411–415 (2011).
44. Armaroli, A. *et al.* Oscillatory dynamics in nanocavities with noninstantaneous Kerr response. *Phys. Rev. A* **84,** 053816 (2011).
45. Johnson, T. J., Borselli, M. & Painter, O. Self-induced optical modulation of the transmission through a high-*Q* silicon microdisk resonator. *Opt. Express* **14,** 817–831 (2006).

Acknowledgements

The authors acknowledge valuable discussions with T.F. Heinz, as well as helpful suggestions from A. Gondarenko, F. Gesuele, Y. Li, J. Lui and J. Yang. The authors acknowledge funding support from NSF IGERT (DGE-1069240) and the Center for Re-Defining Photovoltaic Efficiency through Molecule Scale Control, an Energy Frontier Research Center funded by the US Department of Energy, Office of Science, Office of Basic Energy Sciences (award no. DE-SC0001085).

Author contributions

T.G. and J.F.M. performed the experiments. T.G., N.P., A.V.D.Z. and J.H. prepared the graphene transfer and synthesis. M.Y., G.Q.L. and D.L.K. nanofabricated the membrane samples. T.G. and C.W.W. performed the numerical simulations. T.G. and C.W.W. prepared the manuscript.

Additional information

The authors declare no competing financial interests. Supplementary information accompanies this paper at www.nature.com/naturephotonics. Reprints and permission information is available online at http://www.nature.com/reprints. Correspondence and requests for materials should be addressed to T.G. and C.W.W.

nature photonics

SUPPLEMENTARY INFORMATION

DOI: 10.1038/NPHOTON.2012.147

S1. Dynamic conductivity and optical absorption of graphene

S1.A. Estimating the Fermi level in CVD grown graphene

The Raman spectra are shown in Figure 1b and Figure S1a. The *G* and *2D* band peaks are excited by a 514 nm laser and are located at 1582 cm^{-1} and 2698 cm^{-1} respectively. The Raman spectra are homogeneous within one device, and vary less than 5 cm^{-1} from sample to sample. The Lorentzian lineshape with full-width half-maximum of the *G* (34.9 cm^{-1}) and *2D* (49.6 cm^{-1}) band indicates the graphene monolayer [S1]. The phonon transport properties are represented by the *G* and *2D* peak positions (varying within 1 cm^{-1} over the sample) and the intensity ratios between the *G* and *2D* peaks (fluctuating from 1 to 1.5) which indicate single monolayer and ~ 5×10^{12} cm^{-2} *p*-doping densities. Good uniformity of graphene is also confirmed by the symmetrical single Raman *G* peak [S2].

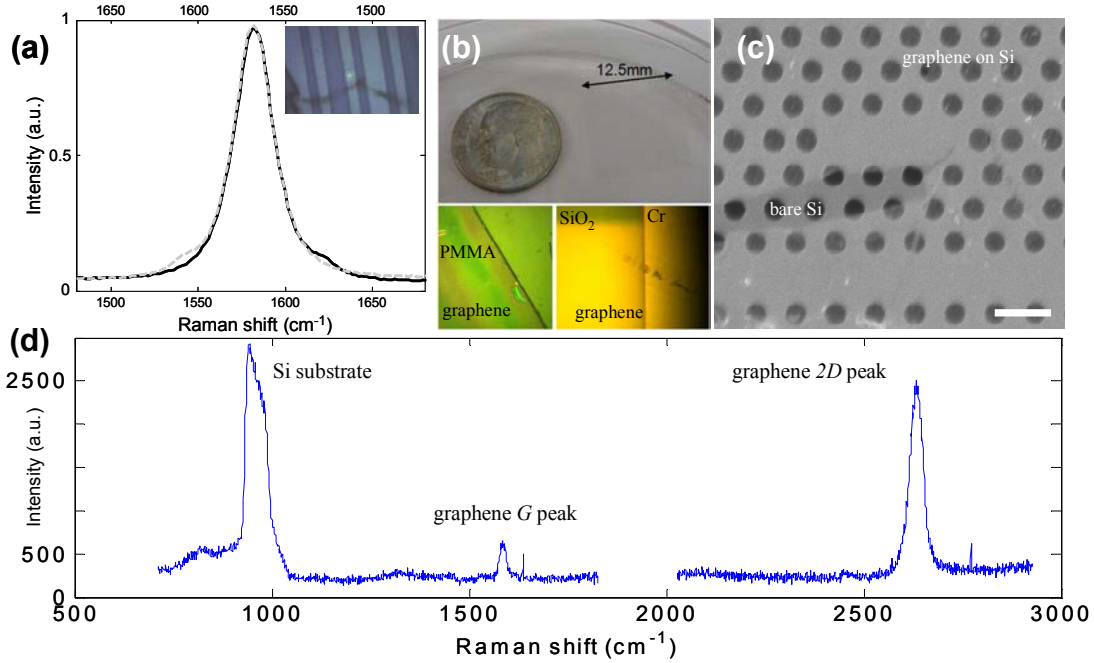

Figure S1 | Raman spectrum and transferred graphene samples. a, Raman *G* peak (black line) and its inverse (grey dashed line) to illustrate *G* peak symmetry. Inset: optical micrograph of the device with graphene transferred under Raman measurement. **b,** A centimeter-scale graphene film prepared. Optical micrograph of graphene film transferred to various substrates (poly-methyl methacrylate), air-bridged silicon membranes, silicon oxide and partially covered metal surfaces), with graphene

DOI: 10.1038/NPHOTON.2012.147

interface pictured. **c,** scanning electronic micrograph of example air-bridged device sample with graphene covering the whole area except the dark (exposed) region. Scale bar: 500 nm. **d,** Complete Raman spectrum of the graphene-cladded silicon membrane samples.

Figure S1b and S1c illustrates example transfers of large-area CVD graphene into various substrates including poly(methyl methacrylate) [PMMA], air-bridged silicon membranes, silicon oxide, and partially covered metal surfaces. CVD grown graphene is thicker and has rough surfaces compared to exfoliated graphene, shown by the broadened *2D* peak and the fluctuation of the *2D* versus *G* peak ratio [S3]. The thickness of graphene is ~ 1 nm. Wrinkles on the graphene surface are formed during the cool down process, due to the differential thermal expansion between the copper substrate and graphene, and consistently appear only at the edges of our samples. We emphasize that at the device regions most of the devices are covered with a single unwrinkled graphene layer.

The *2D* peak is observable only when the laser excitation energy (E_L) and the energy corresponding to electron-hole recombination process (E_T) follow the relation: $(E_L\text{-}E_T)/2 > E_F$, where E_F is the Fermi energy of graphene. With 514 nm laser excitation, the *2D* peak is located at 2698 cm^{-1} (Figure 1b and Figure S1a).

We note that wet transfer of graphene is used in these measurements. While a very thin (in the range of nanometers) residual layer of PMMA can remain on the sample after transfer, PMMA typically only has a non-centrosymmetric $\chi^{(2)}$ response with a negligible $\chi^{(3)}$ response and hence does not contribute to the enhanced four-wave mixing observations. The dopants can arise from residual absorbed molecules or ions on graphene or at the grain boundaries, during the water bath and transfer process. With the same CVD growth process, we also examined the dry transfer technique which controls the doping density to be low enough such that the Fermi level is within the interband optical transition region. In that case, the measured samples have a significantly increased fiber-chip-fiber coupling loss from ~0dB to ~ 11 dB over the 120 μm length photonic crystal waveguide (~0.01dB/μm).The wet transfer technique significantly reduced the linear absorption, thereby allowing the various nonlinear optoelectronic measurements first observed in this work.

S1.B. Calculations of graphene's dynamic conductivity

Given the fact that CVD graphene is heavily *p*-doped, the dynamic conductivity for intra- and inter-band optical transitions [S4] can be determined from the Kubo formalism as:

$$\sigma_{\text{intra}}(\omega) = \frac{je^2\mu}{\pi\hbar(\omega + j\tau^{-1})} \quad , \tag{S-E1}$$

$$\sigma_{\text{inter}}(\omega) = \frac{je^2\mu}{4\pi\hbar}\ln\left(\frac{2|\mu| - \hbar(\omega + j\tau^{-1})}{2|\mu| + \hbar(\omega + j\tau^{-1})}\right), \tag{S-E2}$$

where e is the electron charge, $\hbar$ is the reduced Plank constant, ω is the radian frequency, μ is chemical potential, and τ is the relaxation time (1.2 ps for interband conductivity and 10 fs for intraband conductivity). The dynamic conductivity of intra- and inter-band transitions at 1560 nm are $(-0.07-0.90i)\times10^{-5}$and $(4.15-0.95i)\times10^{-5}$ respectively, leading to the total dynamic conductivity $\sigma_{total}=\sigma_{intra}+\sigma_{inter}$ of $(4.1-1.8i)\times10^{-5}$. Given negative imaginary part of total conductivity, the TE mode is supported in graphene [S5]. The light can travel along the graphene sheet with weak damping and thus no significant loss is observed for the quasi-TE mode confined in the cavity [S6]. The impurity density of the 250 nm silicon membrane is $\sim10^{11}$ cm^{-2}, slightly lower than the estimated doping density in graphene: $\sim5\times10^{12}$ cm^{-2}).

S2. Parameter space of nonlinear optics in graphene nanophotonics

Figure S2 compares cavity-based switching and modulation across different platforms including silicon, III-V and the hybrid graphene- silicon cavities examined in this work. The thermal or free-carrier plasma-based switching energy is given by$P_{0th/e}\times\tau_{th/e}$, where $P_{0th/e}$is the threshold laser power required to shift the cavity resonance half-width through thermal or free carrier dispersion; $\tau_{th/e}$ are the thermal and free-carrier lifetimes in resonator. Note that the lifetime should be replaced by cavity photon lifetime if the latter is larger (for high Q cavity). Graphene brings about a lower switching energy due to strong two-photon absorption (~3,000 cm/GW) [S7]. The recovery times of thermal switching (in red) are also shortened due to higher thermal conductivity in graphene, which is measured for supported graphene monolayers at 600 W/mK [S8] and bounded only by the graphene-contact interface and strong interface phonon scattering.

DOI: 10.1038/NPHOTON.2012.147

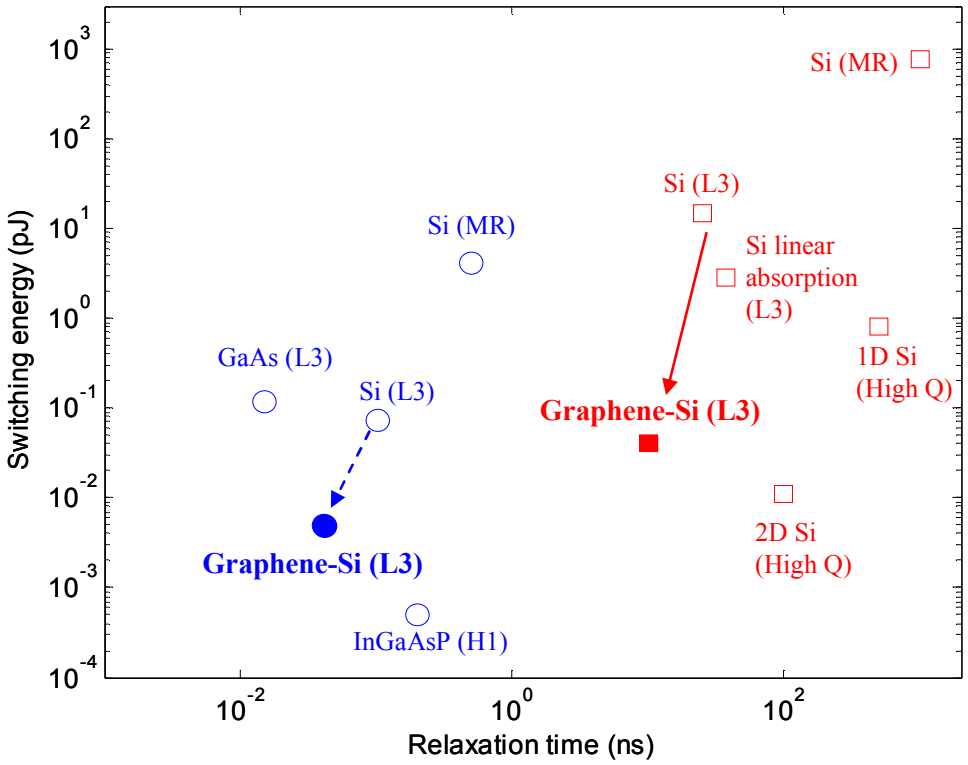

Figure S2 | Comparison of switching energy versus recovery time of cavity-based modulators and switches across different semiconductor material platforms. The blue circles are carrier plasma-induced switches with negative detuning, and the red squares are thermal-optic switches with positive detuning. The dashed lines illustrate the operating switch energies versus recovery times, for the same material [S9-16]. *L3* (*H1*) denotes photonic crystal *L3* (*H1*) cavity; *MR* denotes microring resonator.

The switching energy is inversely proportional to two photon absorption rate (β_2). Table I below summarizes the first-order estimated physical parameters from: (1) coupled-mode theory and experimental data matching; (2) full three-dimensional numerical field simulations, and (3) directly measured data, further detailed in the various sections of this Supplementary Information. With the enhanced two-photon absorption in graphene and first-order estimates of the reduced carrier lifetimes (detailed in Section S3), the switching energy – recovery time performance of the hybrid graphene-silicon cavity is illustrated in Figure S2, compared to monolithic GaAs or silicon ones.

TABLE I | Estimated physical parameters from time-dependent coupled-mode theory-experimental matching, three-dimensional numerical field simulations, and measurement data.

Parameter	Symbol	GaAs [S17]	Si	Monolayer Graphene-Si
TPA coefficient	β_2 (cm/GW)	10.2	1.5 [S18]	25[3D]
Kerr coefficient	n_2 (m^2/W)	1.6×10-17	0.44×10^{-17} [S18]	7.7×10^{-17} [3D]
Thermo-optic coeff.	dn/dT	2.48×10-4	1.86×10^{-4}	
Specific heat	$c_v\rho$(W/Km^{-3})	1.84×106	1.63×10^{6} [cal]	
Thermal relaxation time	$\tau_{th,c}$ (ns)	8.4	12	10 [cal]
Thermal resistance	R_{th} (K/mW)	75	25 [19]	20 [cal]
FCA cross section	σ ($10^{-22}m^3$)	51.8	14.5	
FCD parameter	ζ ($10^{-28}m^3$)	50	13.4	
Carrier lifetime	τ_{fc} (ps)	8	500 [S20]	200 [CMT]
Loaded Q	Q	7000	7000 [m]	
Intrinsic Q	Q_0	30,000	23,000 [m]	

[CMT]: nonlinear time-dependent coupled mode theory simulation; [3D]: three-dimensional numerical field calculation averages; [m]: measurement at low power; [cal]: first-order hybrid graphene-silicon media calculations. τ_{fc} is the effective free-carrier lifetime accounting for both recombination and diffusion.

S3. Graphene two-photon absorption and accompanying thermal and free-carrier nonlinearities

With increasing input power, the transmission spectra evolve from symmetric Lorentzian to asymmetric lineshapes as illustrated in the examples of Figure 1d and Figure S3. Through second-order perturbation theory [S7], the two-photon absorption coefficient β_2 in monolayer graphene is estimated through the second-order interband transition probability rate per unit area as:

$$\beta_2 = \frac{4\pi^2}{\varepsilon_\omega \omega^4 \hbar^3}\left(\frac{v_F e^2}{c}\right)^2 , \qquad \text{(S-E3)}$$

where v_F is the Fermi velocity, $\hbar$ is the reduced Planck's constant, e is the electron charge, and ε_ω is the permittivity of graphene in the given frequency. At our 1550 nm wavelengths, β_2 is determined through Z-scan measurements and first-principle calculations to be in the range of ~ 3,000 cm/GW [S7].

We track the *L3* cavity resonance in the transmission spectra with different input powers as illustrated in Figure S3. With thermal effects, the cavity resonance red-shifts

DOI: 10.1038/NPHOTON.2012.147

1.2 nm/mW for the graphene-cladded sample (Q ~ 7,000) and only 0.3 nm/mW for silicon sample (similar Q ~ 7,500). These sets of measurements are summarized in Figure S3c where the thermal red-shift is sizably larger in the graphene-cladded sample versus a near-identical monolithic silicon cavity. In addition, Figure S3d shows the tuning efficiency for a range of cavity Qs examined in this work – with increasing Q the monolithic silicon cavity shows an increase in tuning efficiency while the converse occurs for the graphene-silicon cavity. Figure S4a shows the steady-state bistable hysteresis for more detunings, and Figure S4b shows the temporal switching with an illustrative detuning of -0.8 and 0.6 nm.

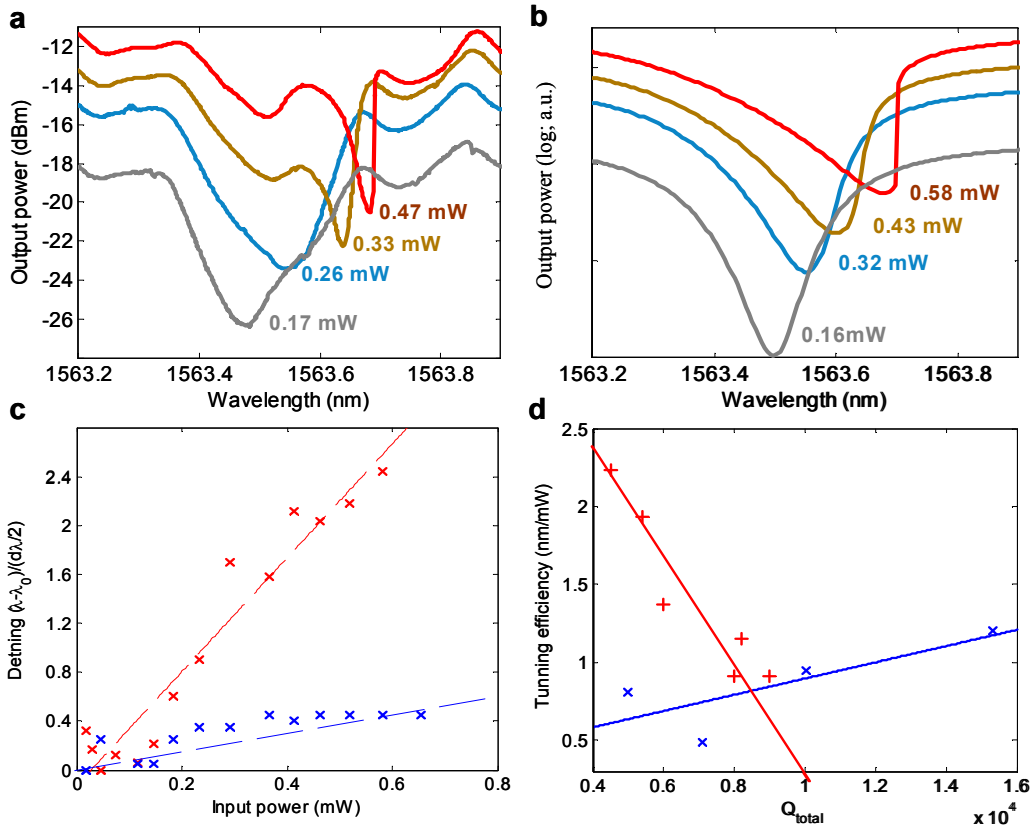

Figure S3 | Steady-state two-photon absorption induced thermal nonlinearities in graphene-silicon hybrid cavities. a, Measured quasi-TE transmission spectra of a graphene-cladded L3 cavity with different input power levels (with extracted insertion loss from the facet of waveguides in order to be comparable to simulation in b). **b,** Nonlinear coupled mode theory simulated transmission spectra. The estimated input powers are marked in the panels. **c,** Measured cavity resonance shifts versus input power, with the graphene-cladded cavity samples (in red) and the monolithic silicon control cavity sample (in blue). **d,** Tuning efficiencies for graphene-cladded cavity samples (in red) and control cavity samples (in blue) for a range of cavity loaded Q-factors examined.

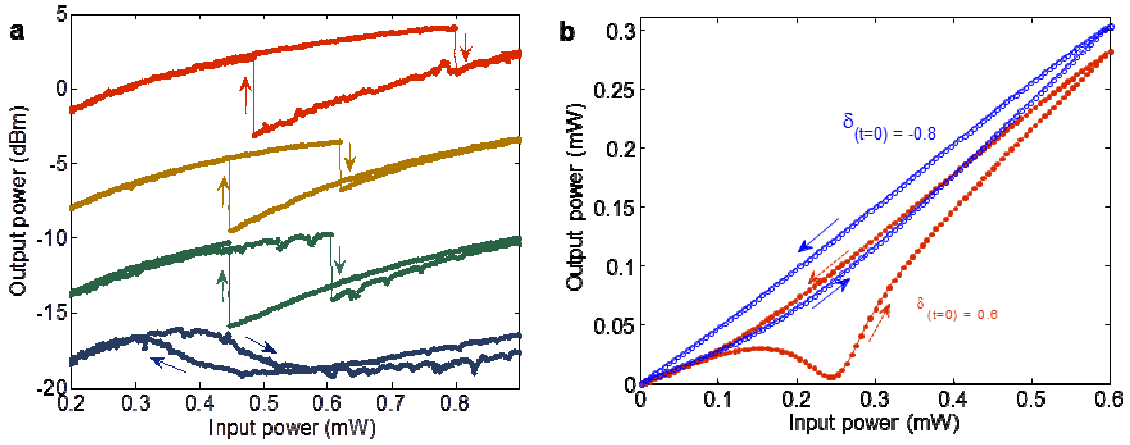

Figure S4 | Bistable switching in graphene-cladded nanocavities. a, Measured steady-state bistability at different detunings set at 0.18, 0.23, 0.26, 0.29 nm (from bottom to top). The plots are offset for clarity: green (offset 2 dB), brown (offset 8 dB) and red lines (offset 15 dB). **b,** Coupled-mode equations calculated switching dynamics with triangular input. The output power versus input power for the positive (red) and negative (blue) detuning with triangular input.

We model the nonlinear cavity transmissions with time-domain nonlinear coupled mode theory for the temporal rate evolution of the photon, carrier density and temperatures as described by [S21]:

$$\frac{da}{dt} = (i(\omega_L - \omega_0 + \Delta\omega) - \frac{1}{2\tau_t})a + \kappa\sqrt{P_{in}}\ , \qquad \text{(S-E4)}$$

$$\frac{dN}{dt} = \frac{1}{2\hbar\omega_0\tau_{TPA}}\frac{V_{TPA}}{V_{FCA}^{\ 2}}|a|^4 - \frac{N}{\tau_{fc}}\ , \qquad \text{(S-E5)}$$

$$\frac{d\Delta T}{dt} = \frac{R_{th}}{\tau_{th}\tau_{FCA}}|a|^2 + \frac{\Delta T}{\tau_{th}}\ , \qquad \text{(S-E6)}$$

where a is the amplitude of resonance mode; N is the free-carrier density; ΔT is the cavity temperature shift. P_{in} is the power carried by incident continuous-wave laser. κ is the coupling coefficient between waveguide and cavity, adjusted by the background Fabry-Perot resonance in waveguide [S22]. ω_L-ω_0 is the detuning between the laser frequency (ω_L) and cold cavity resonance (ω_0). The time-dependent cavity resonance shift is $\Delta\omega=\Delta\omega_N-\Delta\omega_T+\Delta\omega_K$, where the free carrier dispersion is $\Delta\omega_N=\omega_0\zeta N/n$.The thermal induced dispersion is $\Delta\omega_T=\omega_0\Delta T(dn/dT)/n$. $\Delta\omega_K$ is the Kerr dispersion, and is negligibly small compared to the thermal and free-carrier mechanisms.

DOI: 10.1038/NPHOTON.2012.147

The total loss rate is $1/\tau_t = 1/\tau_{in}+1/\tau_v+1/\tau_{lin}+1/\tau_{TPA}+1/\tau_{FCA}$. $1/\tau_{in}$ and $1/\tau_v$is the loss rates into waveguide and vertical radiation into the continuum, ($1/\tau_{in/v} = \omega/Q_{in/v}$), the linear absorption $1/\tau_{lin}$for silicon and graphene are demonstrated to be small. The free carrier absorption rate $1/\tau_{FCA}=c\sigma N(t)/n$. The field averaged two-photon absorption rate$1/\tau_{TPA}=\overline{\beta_2}\, c^2/n^2/V_{TPA}|a|^2$, where the effective two-photon absorption coefficient is defined as:

$$\overline{\beta_2} = (\frac{\lambda_0}{2\pi})^d \frac{\int n^2(r)\beta_2(r)(|E(r)\cdot E(r)|^2 + 2|E(r)\cdot E(r)^*|^2)d^d r}{(\int n^2(r)|E(r)|^2\, d^d r)^2}, \quad \text{(S-E7)}$$

The mode volume for two-photon absorption (same as Kerr):

$$V_{TPA/Kerr} = \frac{(\int n^2(r)|A(r)|^2\, dr^3)^2}{\int_{Si} n^4(r)|A(r)|^4\, dr^3}, \quad \text{(S-E8)}$$

The effective mode volume for free-carrier absorption is:

$$V^2_{FCA} = \frac{(\int n^2(r)|A(r)|^2\, dr^3)^3}{\int_{Si} n^6(r)|A(r)|^6\, dr^3}. \quad \text{(S-E9)}$$

The model shows remarkable match to the measured transmissions. With the two-photon absorption and Kerr (Supplementary Information, Section 5) coefficients of the hybrid cavity calculated from 3D finite-difference time-domain field averages and first-order estimates of the thermal properties (specific heat, effective thermal resistance, and relaxation times), the carrier lifetime of the graphene-cladded photonic crystal cavity is estimated to first-order at 200 ps.

S4. Switching dynamics and regenerative oscillation in graphene-cladded silicon cavities

From the nonlinear coupled mode modeling, the dynamical responses of the hybrid cavity to step inputs are shown in Figure S5a, illustrating the switching dynamics and regenerative oscillations. Free carrier dispersion causes the switching on the negative-detuned laser, and the thermal nonlinearity leads to the switching on the positive side. The interplay of the free-carrier-induced cavity resonance blue-shift dynamics with the thermal-induced cavity red-shift time constants is observed. Figure S5b shows the correspondent radio frequency spectrum. By tuning the laser wavelength, the fundamental mode can be set from 48 MHz (zero detuning) to 55 MHz (0.3 nm detuning). The dependence of oscillation period to the detuning and input laser power is further provided in Figure S5c and Figure S5d respectively.

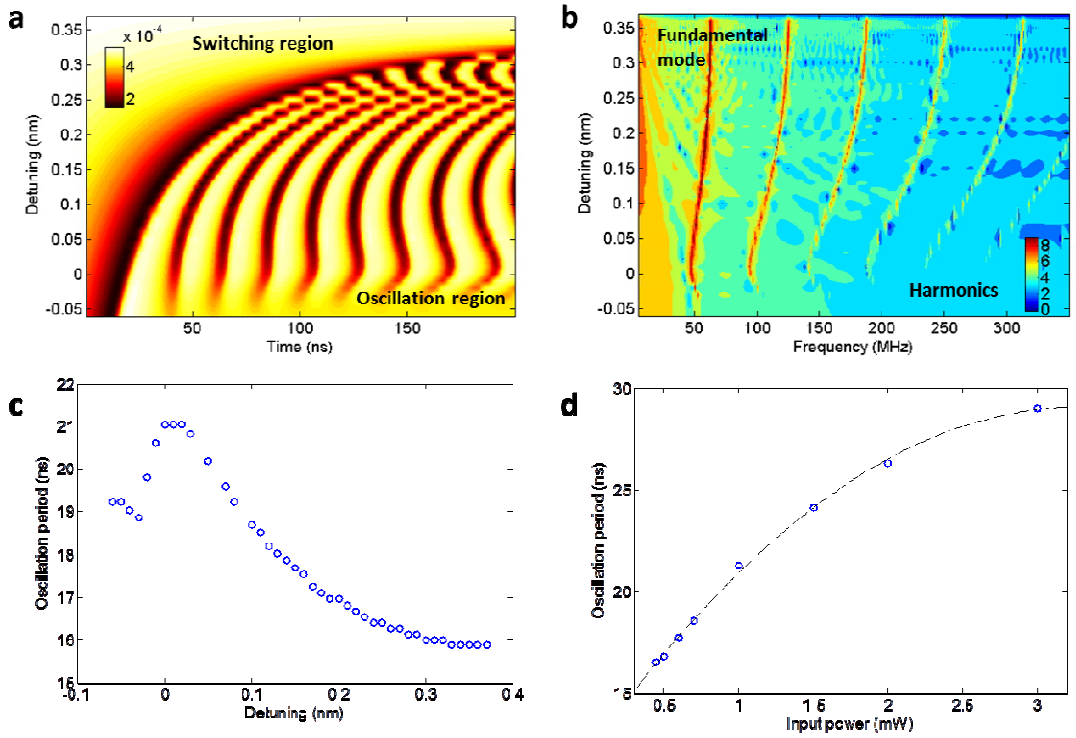

Figure S5 | Coupled-mode equations calculated time domain response to a step input with a graphene-cladded silicon photonic crystal *L3* nanocavity side-coupled to a photonic crystal waveguide. a, The output versus input powers for positive and negative detunings (laser-cavity detunings are set from -0.06 to 0.37 nm). Input laser power is set at 0.6 mW. The cavity switching dip is observed for all detunings, and regenerative oscillation exists only predominantly for positive detuning. **b,** Frequency response of the cavity switching and oscillation dynamics with conditions as in **a** (in log scale). The laser detuning is set from -0.06 to 0.37 nm. **c** and **d.** Oscillation period versus laser detunings and input powers respectively.

Regenerative oscillations were theoretically predicted in GaAs nanocavities with large Kerr nonlinearities [S23], or observed only in high-Q silicon microdisks (Q at 3×10^5) with V at $40(\lambda/n_{Si})^3$, at sub-mW power levels [S24]. The graphene-enhanced two-photon absorption, free-carrier and thermal effects allow regenerative oscillations to be experimentally observable with Q^2/V values [of $4.3\times10^7(\lambda/n)^3$] at least 50× lower, at the same power threshold levels. The regenerative oscillations with lower Qs allow higher speed and wider bandwidth operation, and are less stringent on the device nanofabrication.

DOI: 10.1038/NPHOTON.2012.147

S5. Ultrafast Kerr in graphene – silicon hybrid structures

S5.A. Computations of effective Kerr nonlinearity in graphene-cladded silicon cavities

Third-order nonlinearity susceptibility for graphene is reported as large as $|\chi^{(3)}|\sim10^{-7}$esu in the wavelength range of 760 to 840 nm [S25]. When two external beams with frequency ω_1 (pump) and ω_2 (signal) are incident on graphene, the amplitude of sheet current generated at the harmonics frequencies ($2\omega_1$-ω_2) is described by:

$$j_e = -\frac{3}{32}\frac{e^2}{\hbar}\varepsilon_2\left(\frac{ev_F\varepsilon_1}{\hbar\omega_1\omega_2}\right)^2\frac{2\omega_1^2+2\omega_1\omega_2-\omega_2^2}{\omega_1(2\omega_1-\omega_2)}\ , \qquad \text{(S-E10)}$$

whereε_1, ε_2 are the electric field amplitudes of the incident light at frequencies ω_1 and ω_2 respectively. v_F (=10^6 m/s) is the Fermi velocity of graphene. Under the condition that both ω_1 and ω_2 are close to ω, the sheet conductivity can be approximated as:

$$\sigma^{(3)} = \frac{j_e}{\varepsilon_1\varepsilon_1\varepsilon_2} = -\frac{9}{32}\frac{e^2}{\hbar}\left(\frac{ev_F}{\hbar\omega^2}\right)^2, \qquad \text{(S-E11)}$$

Since most of the sheet current is generated in graphene, the effective nonlinear susceptibility of the whole membrane can be expressed as:

$$\chi^{(3)} = \frac{\sigma^{(3)}}{\omega d} = -\frac{9}{32}\frac{e^4 v_F{}^2}{\hbar^3 c^5}\frac{\lambda^5}{d}, \qquad \text{(S-E12)}$$

where d is the thickness of the graphene (~1 nm), λ is the wavelength, and c is the speed of light in vacuum. The calculated $\chi^{(3)}$ of a monolayer graphene is in the order of 10^{-7}esu (corresponding to a Kerr coefficient $n_2\sim 10^{-13}$ m^2/W), at 10^5 times higher than in silicon ($\chi^{(3)}\sim 10^{-13}$esu, $n_2\sim 4\times10^{-18}$ m^2/W) [S26].

Effective $n_2$of the hybrid graphene-silicon membrane is then calculated for an inhomogeneous cross-section weighted with respect to field distribution [S27]. With a baseline model without complex graphene-surface electronic interactions, the effective n_2 can be expressed as:

$$\overline{n_2} = \left(\frac{\lambda_0}{2\pi}\right)^d \frac{\int n^2(r)n_2(r)(|E(r)\cdot E(r)|^2+2|E(r)\cdot E(r)^*|^2)d^dr}{(\int n^2(r)|E(r)|^2\,d^dr)^2}, \qquad \text{(S-E13)}$$

where $E(r)$ is the complex fields in the cavity and $n(r)$ is local refractive index. The local Kerr coefficient $n_2(r)$ is 3.8×10^{-18} m^2/W in silicon membrane and ~10^{-13} m^2/W for graphene, λ_0 is the wavelength in vacuum, and $d=3$ is the number of dimensions. The complex electric field $E(r)$ is obtained from 3D finite-difference time-domain computations of the optical cavity examined [S28]. The resulting field-balanced effective n_2 is calculated to be 7.7×10^{-17} m^2/W ($\chi^{(3)}\sim 10^{-12}$esu), close to the best reported chalcogenide photonic crystal waveguides [S29, S30].

TABLE II | Field-balanced third-order nonlinear parameter.

Computed parameters	$\overline{n_2}$ (m^2/W)	$\overline{\beta_2}$ (m/W)
Graphene	10^{-13}	10^{-7}
Silicon	3.8×10^{-18}	8.0×10^{-12}
Monolayer graphene-silicon	7.7×10^{-17}	2.5×10^{-11}
Chalcogenide waveguide	7.0×10^{-17}	4.1×10^{-12}

Likewise, the effective two-photon absorption coefficient is computed in the same field-balanced approach, with a result of 2.5×10^{-11}m/W. The resulting nonlinear parameter γ ($=\omega n_2/cA_{eff}$) is derived to be 800 W^{-1}m^{-1}, for an effective mode area of 0.25 μm^2.

S5.B. Local four-wave mixing in graphene-cladded photonic crystals cavities

The conversion efficiency of the single cavity $\eta=|\gamma P_p L'|^2 FE_p^4 FE_s^2 FE_c^2$, where FE_p, FE_s, and FE_c are the field enhancement factors of pump, signal and idler respectively [S31]. The effective length L' includes the phase mismatch and loss effects. Compared to the original cavity length (~ 1582.6 nm), the effective cavity length is only slightly modified by less than 1 nm. However, the spectral dependent field enhancement factor is the square of the cavity build-up factor $FE^2=P_{cav}/P_{wg}=F_{cav}(U/U_{max})\eta_p^2$, where U/U_{max} is the normalized energy distribution with the Lorenzian lineshape. η_p=0.33 is the correction term for the spatial misalignment between the quasi-TE mode and graphene, and the polarization. The field enhancement effect in the cavity is proportional to the photon mode density: $F_{cav}=Q\lambda^3/(8\pi V)$ [S32].

DOI: 10.1038/NPHOTON.2012.147

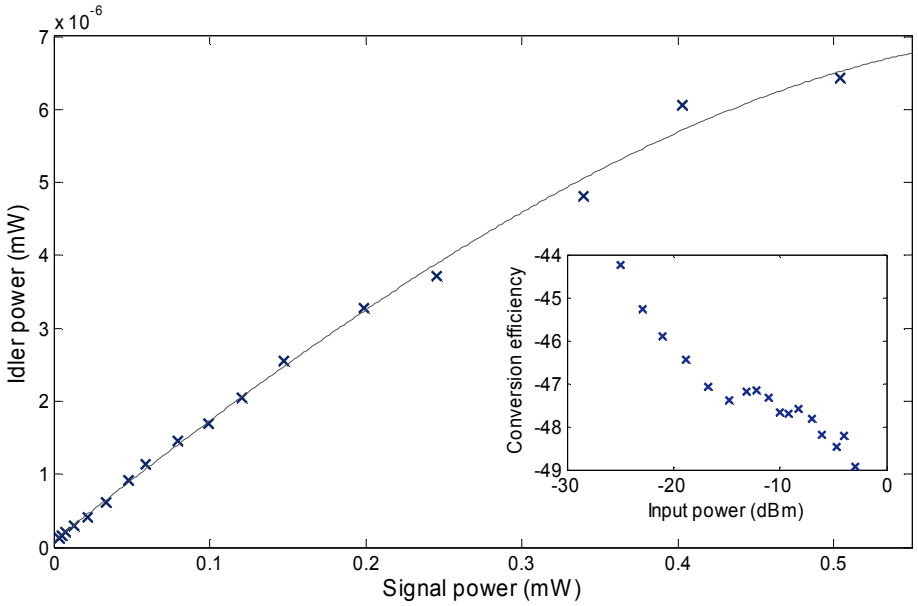

Figure S6 | Free-carrier absorption effects on the four-wave mixing conversion efficiency. Measured idler power versus signal power at the transmitted port, with the pump power is fixed on the cavity resonance and the the signal laser detuned by 200 pm. Experimental data (×) and quadratic fit (solid line). Inset: corresponding conversion efficiency versus signal power.

The enhanced two-photon-absorption and induced free-carrier absorption would produce nonlinear loss. To investigate the direct effect of two-photon absorption and free-carrier absorption on the four wave mixing, we measure the conversion efficiency with varying input signal power as shown in Figure S6. Extra 4-dB loss is measured when the input signal power increases from -22 to -10 dBm, with the additional contribution from nonlinear absorption of the graphene-silicon cavity membrane.

Supplementary References:

[S1] A. Das, S. Pisana, B. Chakraborty, S. Piscanec, S. K. Saha, U. V. Waghmare, K. S. Novoselov, H. R. Krishnamurthy, A. K. Geim, A. C. Ferrari, and A. K. Sood, Monitoring dopants by Raman scattering in an electrochemically top-gated graphene transistor, *Nature Nanotech.* **3**, 210 (2008); C. Casiraghi, S. Pisana, K. S. Novoselov, A. K. Geim, and A. C. Ferrari, Raman fingerprint of charged impurities in graphene, *Appl. Phys. Lett.* **91**, 233108 (2007).

[S2] X. Li, W. Cai, J. An, S. Kim, J. Nah, D. Yang, R. Piner, A. Velamakanni, I. Jung, E. Tutuc, S. K. Banerjee, L. Colombo, and R. S. Ruoff, Large-area synthesis of

high-quality and uniform graphene films on copper foils, *Science* **324**, 1312 (2009).

[S3] W. Zhao, P. H. Tan, J. Liu, and A. C. Ferrari, Intercalation of few-layer graphite flakes with $FeCl_3$: Raman determination of Fermi level, layer by layer decoupling, and stability, *J. Am. Chem. Soc.* **133**, 5941 (2011).

[S4] K.F. Mak, M.Y. Sfeir, Y. Wu, C.H. Lui, J.A. Misewich, and T.F. Heinz, Measurement of the Optical Conductivity of Graphene, *Phys. Rev. Lett.* **101**, 196405 (2008).

[S5] Q. Bao, H. Zhang, B. Wang, Z. Ni, C. H. Y. X. Lim, Y. Wang, D. Yuan Tang, and K. P. Loh, Broadband graphene polarizer, *Nature Photon.* **5**, 411 (2011).

[S6] S. Mikhailov and K. Ziegler, New electromagnetic mode in graphene. *Phys. Rev. Lett.* **99**, 016803 (2007).

[S7] H. Yang, X. Feng, Q. Wang, H. Huang, W. Chen, A. T. S. Wee, and W. Ji, Giant two-photon absorption in bilayer graphene, *Nano Lett.* **11**, 2622 (2011).

[S8] J. H. Seol, I. Jo, A. L. Moore, L. Lindsay, Z. H. Aitken, M. T. Pettes, X. Li, Z. Yao, R. Huang, D. Broido, N. Mingo, R. S. Ruoff, and L. Shi, Two-dimensional phonon transport in supported graphene, *Science* **328**, 213 (2010).

[S9] T. Tanabe, M. Notomi, S. Mitsugi, A. Shinya, and E. Kuramochi, Fast bistable all-optical switch and memory on a silicon photonic crystal on-chip, *Opti. Lett.* **30**, 2575 (2005).

[S10] M. Notomi, A. Shinya, S. Mitsugi, G. Kira, E. Kuramochi, and T. Tanabe, Optical bistable switching action of Si high-Q photonic-crystal nanocavities, *Opt. Express* **13**, 2678 (2005).

[S11] L.-D. Haret, T. Tanabe, E. Kuramochi, and M. Notomi, Extremely low power optical bistability in silicon demonstrated using 1D photonic crystal nanocavity, *Optics Express* **17**, pp. 21108 (2009).

[S12] K. Nozaki, T. Tanabe, A. Shinya, S. Matsuo, T. Sato, H. Taniyama, and M. Notomi, Sub-femtojoule all-optical switching using a photonic crystal nanocavity, *Nature Photon.* **4**, 477 (2010).

DOI: 10.1038/NPHOTON.2012.147

[S13] C. Husko, A. De Rossi, S. Combrié, Q. V. Tran, F. Raineri, and C. W. Wong, Ultrafast all-optical modulation in GaAs photonic crystal cavities, *Appl. Phys. Lett.* **94**, 021111 (2009).

[S14] S. Kocaman, X. Yang, J. F. McMillan, M. B. Yu, D. L. Kwong, and C. W. Wong, Observations of temporal group delays in slow-light multiple coupled photonic crystal cavities, *Appl. Phys. Lett.* **96**, 221111 (2010).

[S15] V. R. Almeida and M. Lipson, Optical bistability on a silicon chip, *Opt. Lett.* **29** 2387 (2004).

[S16] Q. Xu and M. Lipson, Carrier-induced optical bistability in silicon ring resonators, *Opt. Lett.* **31**, 341 (2006).

[S17] A. de Rossi, M. Lauritano, S. Combrie, Q. Vy Tran, and C. Husko, Interplay of plasma-induced and fast thermal nonlinearities in a GaAs-based photonic crystal nanocavity, *Phys. Rev. A* **79**, 043818 (2009).

[S18] Alan D. Bristow, Nir Rotenberg, and Henry M. van Driel, Two-photon absorption and Kerr coefficients of silicon for 850–2200 nm, *Appl. Phys. Lett.* **90**, 191104 (2007).

[S19] C. J. Chen, J. Zheng, T. Gu, J. F. McMillan, M. Yu, G.-Q. Lo, D.-L. Kwong, and C. W. Wong, Selective tuning of silicon photonic crystal nanocavities via laser-assisted local oxidation, *Optics Express* **19**, 12480 (2011).

[S20] P. E. Barclay, K. Srinivasan, and O. Painter, Nonlinear response of silicon photonic crystal micro-resonators excited via an integrated waveguide and fiber taper, *Opt. Express* **13**, 801 (2005).

[S21] H. A. Haus, *Waves and Fields in Optoelectronics* (Prentice-Hall, Englewood Cliffs, NJ), p. 99 (1984).

[S22] X. Yang, C. Husko, M. Yu, D.-L. Kwong, and C. W. Wong, Observation of femto-joule optical bistability involving Fano resonances in high-Q/V_m silicon photonic crystal nanocavities, *Appl. Phys. Lett.* **91**, 051113 (2007).

[S23] A. Armaroli, S. Malaguti, G. Bellanca, S. Trillo, A. de Rossi, and S. Combrié, Oscillatory dynamics in nanocavities with noninstantaneous Kerr response, *Phys. Rev. A* **84**, 053816 (2011)

[S24] T. J. Johnson, M. Borselli, and O. Painter, Self-induced optical modulation of the transmission through a high-*Q* silicon microdisk resonator, *Opt. Express* **14**, 817 (2006).

[S25] E. Hendry, P.J. Hale, J. Moger, and A. K. Savchenko, Coherent nonlinear optical response of graphene, *Phys. Rev. Lett.***105**, 097401 (2010).

[S26] M. Dinu, F. Quochi, and H. Garcia, Third-order nonlinearities in silicon at telecom wavelengths, *Appl. Phys. Lett.* **82**, 2954 (2003).

[S27] S. Afshar V. and T. M. Monro, A full vectorial model for pulse propagation in emerging waveguides with subwavelength structures part I: Kerr nonlinearity, *Optics Express* **17**, 2298 (2009).

[S28] A. F. Oskooi, D. Roundy, M. Ibanescu, P. Bermel, J. D. Joannopoulos, and S. G. Johnson, MEEP: A flexible free-software package for electromagnetic simulations by the FDTD method, *Computer Physics Communications* **181**, 687 (2010).

[S29] B. J. Eggleton, B. Luther-Davies and K. Richardson, Chalcogenide photonics, *Nature Photonics* **5**, 141 (2011).

[S30]K. Suzuki, Y .Hamachi, and T. Baba, Fabrication and characterization of chalcogenide glass photonic crystal waveguides. *Opt. Express* **17**, 22393 (2009).

[S31] P. P. Absil, J. V. Hryniewicz, B. E. Little, P. S. Cho, R. A. Wilson, L. G. Joneckis, and P.-T. Ho, Wavelength conversion in GaAs micro-ring resonators, *Opt. Lett.* **25**, 554 (2000).

[S32] R. K. Chang and A. J. Campillo, *Optical processes in microcavities*, World Scientific, Singapore, 1996.

NONLINEAR OPTICS

Graphene–silicon fusion

A single sheet of graphene dramatically changes the nonlinear response of a silicon photonic crystal, enabling ultralow-power optical bistability, self-induced regenerative oscillation and coherent four-wave mixing.

Kinam Kim, Seong-Ho Cho, and Chang-Won Lee

The realization of an ultrafast, all-optical switching device has long been a goal for scientists in the field of optical information technology. In 2010, researchers successfully demonstrated an optical switch based on the nonlinear optical response of a high-Q photonic crystal structure, which was made possible by the maturation of silicon fabrication technology[1]. Unfortunately, the low optical nonlinear coefficients of silicon and group III–V materials caused the final device to exhibit extremely narrow operating margins. The need for a wide operating margin has made it very difficult to realize a micro- or nanocavity capable of exhibiting nonlinear responses.

Reporting in *Nature Photonics*, Tingyi Gu and co-workers from Columbia University in the USA and the Institute of Microelectronics in Singapore have demonstrated that placing a sheet of graphene on top of the silicon photonic crystal structure can significantly enhance its nonlinear response[2].

The zero-bandgap linear electronic band structure of graphene — known as the Dirac-cone — has been studied for its potential use throughout a wide range of optoelectronic applications[3]. Graphene's linear dispersion provides a universal light absorption of around 2.3% from infrared to visible wavelengths. Therefore, unlike other semiconductor-based photonic devices, graphene can in principle be used to achieve ultrabroadband operation.

Gu *et al.* exploited an intriguing but lesser-known property of graphene: its optical nonlinearity[2]. In a previous study, Hendry *et al.* reported the use of graphene flakes in four-wave mixing[4]. They found that the nonlinear susceptibility $\chi^{(3)}$ of the graphene flakes was 10^{-7} esu, which is two orders of magnitude higher than that of a 4-nm-thick gold film. This value is 10^5 times higher than the values reported for silicon[5] — no other material has shown a nonlinear coefficient comparable to that of graphene. The peculiar electronic band structure of graphene enables all interband transitions to be resonant[6]. Low-carrier concentration and easy band filling provide very low-power saturated absorption, leading to mode-locking operation and hence to ultrafast pulsed laser operation[7,8].

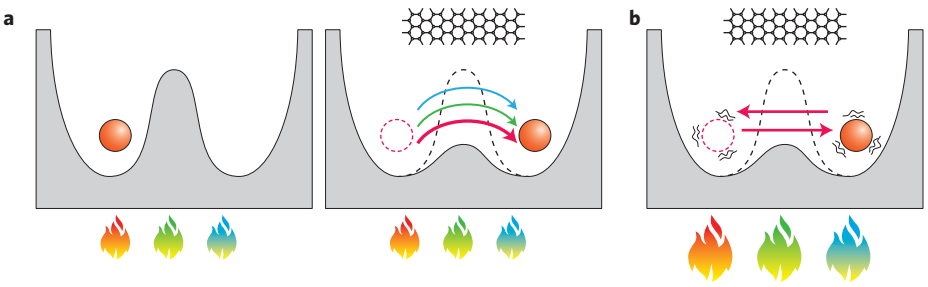

Figure 1 | Double-well model of excitation-dependent nonlinear optical phenomena in a graphene–silicon hybrid system. **a**, A graphene-on-silicon photonic crystal cavity reduces the potential barrier to facilitate optical bistability during heating. The colours of each flame represent the detuned wavelengths of the input laser. **b**, Increased heating power induces regenerative oscillation between the two potential wells.

The researchers chose to exploit the best features of both approaches: the large Q-factor of a silicon photonic crystal and the large nonlinearity of graphene. For a nonlinear response to be effective, the electromagnetic field inside the cavity must be captured and maintained using a photonic crystal with a very high Q-factor. However, in this approach, the fabrication tolerance is extremely narrow. Graphene, in contrast, does not require an ultrahigh Q-factor to induce a suitable nonlinearity in the cavity. Gu *et al.* adopted a silicon photonic crystal cavity scheme designed by Akahane *et al.*, the result of which showed an intrinsic Q-factor of 23,000 and a loaded Q-factor of 7,500 (ref. 9).

In order to convert the $\chi^{(3)}$ susceptibility of the hybrid structure into a straightforward nonlinear Kerr coefficient (n_2), the team employed a four-wave mixing set-up and a vectorial model that relied on finite-difference time-domain calculations. They obtained a value of $n_2 = 7.7 \times 10^{-17}$ m^2 W^{-1}, which is 17 times larger than that of silicon with the same structure and is similar to that of chalcogenide glass on a silicon photonic structure (7.0×10^{-17} m^2 W^{-1}; ref. 10). The hybrid graphene–silicon structure also exhibited an estimated threshold cavity energy of hundreds of attojoules.

This enhanced nonlinearity allowed Gu *et al.* to demonstrate two interesting behavioural aspects of the graphene–silicon hybrid structure: steady-state optical bistability and regenerative oscillation, both of which can be understood by considering a ball oscillating in a double potential well (Fig. 1). In this analogy, the ball is being heated by an external source (the laser). Without graphene, the potential barrier is too high for the ball to jump into the next well. The role of graphene is to lower the potential barrier and thus allow the ball to jump over the wall (Fig. 1a). The researchers observed input–output optical bistability in both steady-state and pulsed-mode operation, even at modest Q-factors. Owing to fast carrier relaxation followed by slow thermal relaxation, only the positive detuning mode showed bistability during the quasi-steady-state sweeping of the input power.

Increasing the input power causes the ball to bounce back and forth — a phenomenon known as regenerative oscillation (Fig. 1b). This oscillatory behaviour usually takes place under a high-intensity pulsed mode. In the graphene–silicon hybrid device, however, this regenerative oscillation appeared even

in a quasi-steady-state pumping condition with triangular input modulation due to competition between phonon (~10 ns) and carrier (~200 ps) relaxation. Gu *et al.* observed an oscillation period of 106 MHz, which will be useful for generating microwaves. This oscillation period differs from the theoretical coupled-mode theory value of 50 MHz due to insufficient information in the model, including a lack of knowledge about the time-varying *Q*-factor of the cavity.

The work of Gu *et al.* provides a very interesting outlook. The development of suitable fabrication techniques should allow graphene sheets to be placed between identical vertically stacked photonic cavities to achieve better mode-overlapping. Graphene sheets could also be used to reduce the threshold power of all-optical nonlinear switches and to achieve non-degenerate optical parametric generation. Graphene may be one of the simplest solid-state materials, but its wealth of fascinating behaviour continues to surprise us, year after year. ❐

Kinam Kim, Seong-Ho Cho and Chang-Won Lee are at Samsung Electronics, San 14, Nongseo-dong, Giheung-gu, Yongin-si, Gyeonggi-do 446-712, Korea.
e-mail: kn_kim@samsung.com

References

1. Nozaki, K. *et al. Nature Photon.* **4,** 477–483 (2010).
2. Gu, T. *et al. Nature Photon.* **6,** 554–559 (2012).
3. Bonaccorso, F., Sun, Z., Hasan, T. & Ferrari, A. C. *Nature Photon.* **4,** 611–622 (2010).
4. Hendry, E., Hale, P. J., Moger, J. & Savchenko, A. K. *Phys. Rev. Lett.* **105,** 097401 (2010).
5. Dinu, M., Quochi, F. & Garcia, H. *Appl. Phys. Lett.* **82,** 2954–2956 (2003).
6. Mikhailov, S. A. *Physica E* **44,** 924–927 (2012).
7. Sun, Z. *et al. ACS Nano* **4,** 803–810 (2010).
8. Huang, P. L. *et al. Opt. Express* **20,** 2460–2465 (2012).
9. Akahane, Y., Asano, T., Song, B.-S. & Noda, S. *Nature* **425,** 944–947 (2003).
10. Eggleton, B. J., Luther-Davies, B. & Richardson, K. *Nature Photon.* **5,** 141–148 (2011).

MICROANALYSIS

Single-atom X-ray spectroscopy

Advances in electron optics and X-ray detection are opening up the periodic table to one of the ultimate goals of microanalysis — single-atom spectroscopy.

Michael Walls

The electron microscope is used both as a microanalytical tool and to produce high-resolution micrographs. Energy-dispersive X-ray spectroscopy (EDX; confusingly also known by a number of different acronyms, including EDS and EDXS) is one of the principal spectroscopic techniques used to identify and quantify chemical species in transmission electron microscopy. The technique involves measuring the energies of X-rays emitted by the targeted region of a sample under an incident electron beam. Peaks in the spectrum correspond to specific electronic transitions and thus yield chemical information about the sample. Writing in *Nature Photonics*, Suenaga *et al.* have now taken on what might be considered the ultimate challenge for a microspectroscopic technique such as EDX: detecting the signal from a single atom[1]. Similar experiments on silicon and platinum atoms were also recently reported by Lovejoy *et al.*[2]

In recent years, researchers have made significant improvements to transmission electron microscopy — particularly for devices operating in scanning mode. Among the many technological breakthroughs, perhaps the most important was the introduction of spherical aberration correctors, which enabled the generation of high-current sub-ångström-sized electron probes and thus opened up the path towards atomic-resolution spectroscopy[3].

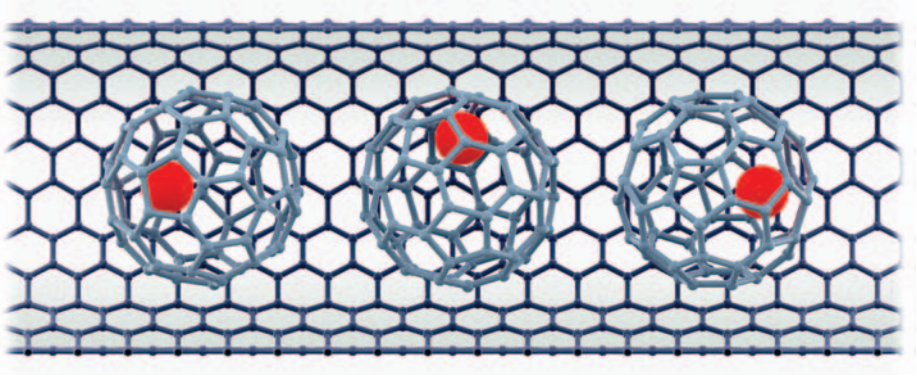

Figure 1 | The 'peapod' structure of Suenaga *et al.*: single erbium atoms trapped within fullerene cages.

Another spectroscopic technique typically employed in transmission electron microscopy is electron energy-loss spectroscopy (EELS), which involves measuring the energy loss of the fast electrons that have traversed the thin sample (usually no more than a few tens of nanometres). EELS has conventionally been considered as the more 'advanced' technique, particularly owing to its vastly superior energy resolution (<1 eV, compared with >100eV for EDX), but it is more difficult to apply and interpret. EELS was also the first technique used to map individual chemical species with atomic spatial resolution in crystals[4]. For many years, researchers assumed that EDX would never have the same spatial resolution as EELS, given the limitations that arise not only from the size of the probe that can be generated, but also from its interaction volume in a sample, which was thought to be much larger in EDX than in EELS. However, recent work has clearly overturned that assumption: the first atomic-resolution EDX maps were demonstrated around two years ago, showing (albeit faintly) individual columns of atoms in aligned crystals[5]. Since then, researchers have continued to improve the quality of the maps produced by EDX. This is due partly to great improvements in spectrometer sensitivities and speeds,